Chemical-shift imaging in micro- and nano-MRI

Rosmarie Joss, Ivan T. Tomka, Kai W. Eberhardt, Jacco D. van Beek, and Beat H. Meier*
Physical Chemistry, ETH Zurich, CH-8093 Zurich, Switzerland
(Received 14 June 2011; revised manuscript received 11 August 2011; published 20 September 2011)

We demonstrate chemical-shift imaging of solids with a spatial resolution of about 1 μm using magnetic resonance force microscopy. Images with two spatial dimensions and one spectral dimension were recorded and an extension to three spatial dimensions and several spectral dimensions is possible. To reduce the measurement time multiplexing schemes are used for all dimensions (by either a Fourier or a Hadamard method) and quadrature detection is introduced for the directly acquired spatial dimension, in combination with Hadamard encoding.

DOI: 10.1103/PhysRevB.84.104435 PACS number(s): 76.60.Pc, 76.60.Cq

I. INTRODUCTION

Magnetic resonance imaging (MRI) is a widely used noninvasive imaging technique.[1] The high sensitivity of nuclear spins to their surrounding chemical environment makes it attractive to add one or several spectral dimensions to the usual spatial dimensions. One example is chemical-shift imaging (CSI),[2] where two or three spatial dimensions are combined with one or more spectral dimensions that characterize the chemical composition at each point of the (conventional) spatial image. While the main applications are doubtlessly in the medical field, MRI has also been applied to soft solids. Typically a spatial resolution of roughly 1 mm is used in medical applications, but resolution down to 1 μm has been achieved in favorable cases.[3,4] In liquid samples with narrow resonance lines, the resolution is essentially limited by the signal-to-noise ratio (SNR) of the experiment, but in solids, with considerably broader resonance lines, the strength of the applicable field gradient is a further limitation.

Both issues can be addressed with magnetic resonance force microscopy (MRFM), which detects spin magnetization via a mechanical sensor: a sample with nuclear or electron magnetic moments is placed in a high magnetic field with a strong field gradient, typically produced by a small ferromagnet positioned close to the sample.[5–8] Compared to inductively detected MRI, MRFM has more favorable scaling behavior with decreasing sample size. It yields a higher sensitivity[9] and even single-electron-spin detection has already been demonstrated.[10] Recently, a nuclear spin image of tobacco mosaic virus with a resolution smaller than 10 nm was demonstrated at cryogenic temperature.[11]

MRI and MRFM are based on the linear relationship between the magnetic field strength and the resonance frequency of the spins, $\omega(\vec{r}) = -\gamma B(\vec{r})$, where γ is the gyromagnetic ratio, B denotes the strength of the applied magnetic field, and $\vec{r}$ is the position vector of the volume element (voxel) described. Therefore, measurement of the resonance frequency in the presence of a magnetic field gradient leads to a one-dimensional spatial localization of the magnetic moment. The power of NMR spectroscopy is based on further and much smaller interactions that influence the resonance frequency ω, namely, the chemical shift, dipolar couplings, scalar couplings, and, for spins with $I > 1/2$, the quadrupole coupling.[12] These interactions may be used to introduce chemical contrast into magnetic resonance images and all of them have, in fact, been demonstrated also in MRFM.[13–18] The chemical-shift interaction probes the electronic environment and allows us to distinguish nuclei that are chemically distinct. It is arguably the most important interaction in chemical, biological, and medical applications. The basic principle of using the chemical shift with MRFM, by mechanically flipping away the gradient source during the chemical-shift evolution period, has recently been demonstrated.[18] Alternative methods have been described elsewhere.[19] This yields so-called localized spectra, meaning NMR spectra for a restricted volume element in the sample.

Here we demonstrate CSI and the use of the chemical shift in nano-MRI to obtain chemical image contrast and describe fast imaging methods that include the chemical-shift interaction, either as an independent spectral dimension or as a filter to obtain contrast in one-dimensional (1D) or 2D spatial images. Hadamard encoding[20–22] in one spatial domain is used to increase the SNR per unit time, as described earlier,[23] and we present a novel quadrature approach that allows a further factor 2 reduction in the measurement time. We apply these methods to a phantom sample, a set of crystals of KPF_6 and MgF_2, and show how spatially localized chemical-shift spectra and 2D spatial images with chemical-shift contrast or a chemical-shift spectrum can be used to study solids by nano-MRI.

II. ENCODING AND RECONSTRUCTION SCHEMES

In this section we introduce different approaches to the measurement of localized chemical-shift spectroscopy, chemical-shift contrast, or CSI and discuss their respective advantages and disadvantages. In order to incorporate chemical-shift information into MRFM images we move the gradient source sufficiently far away from the sample during the relevant period of the experiment, thereby obtaining a homogeneous field for high-resolution spectroscopy.[18] The setup used in the experiments presented here is shown schematically in Fig. 1.

To minimize measurement times, all spectral dimensions were recorded using multiplexing schemes choosing either Fourier (see Sec. II A) or Hadamard (see Sec. II B) encoding. For the spatial z dimension, encoded by the B_0 gradient produced by a ferromagnetic gradient source (Fig. 1), Hadamard encoding yields the optimum sensitivity per unit time.[23] We also describe, in the following, a novel extension of the Hadamard scheme in the form of a quadrature detection scheme (Sec. II C).

To denominate the various experiments we define the following shorthand notation for each dimension of the images, X^{exp}, where X denotes the encoding scheme, and exp the

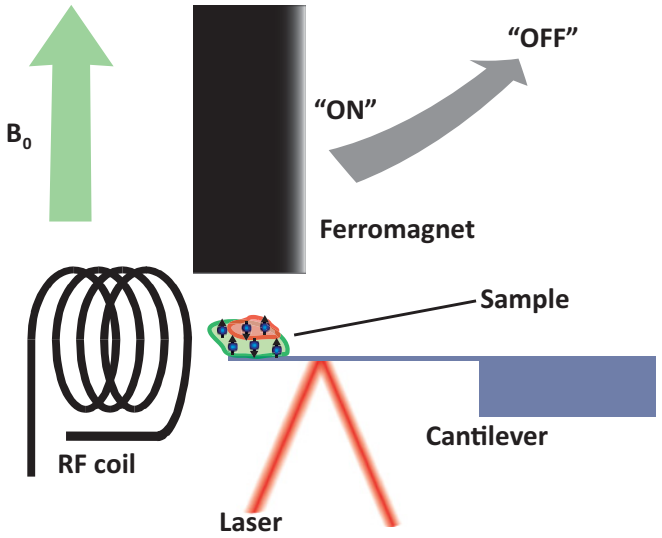

FIG. 1. (Color online) Schematic of the MRFM setup. The sample, consisting here of MgF_2 (red; encircled by small oval within larger oval) and KPF_6 (green) crystals, is glued onto the cantilever. Depending on the spin orientation, the sample experiences an attractive or repulsive force due to the ferromagnetic gradient source placed over the sample. The spins are inverted periodically using radio-frequency irradiation at the mechanical resonance frequency of the cantilever. The resulting cantilever oscillation is detected by a laser-beam deflection sensor. To achieve a homogeneous magnetic field for spectroscopic encoding in the imaging experiments, a piezo bender is included in the setup, which can flip the gradient source away from the sample position.

type of dimension. The encoding scheme can be H_N, H_{Nq}, F, or S which stand for Hadamard-N encoding, quadrature Hadamard-N encoding, Fourier encoding, and slice-by-slice readout, respectively. The types of dimensions are denoted "spa" and "spe," short for spatial and spectral dimension, respectively.

A. Fourier transform (FT) chemical-shift imaging

FT-CSI experiments $F^{\mathrm{spe}}S$ are measured with the pulse sequence shown in Fig. 2(a). The chemical shift is encoded during t_1 evolution, in which a magic echo is applied to refocus the dipolar interaction.[24] The phase cycle $\{\mathrm{y},-\mathrm{y}\}$ of the first $\pi/2$ pulse ensures the required amplitude modulation and further suppresses remaining radio-frequency (rf) cantilever interactions. Phase sensitivity in the spectral dimension is achieved by applying TPPI.[25] The signal is detected slice by slice using a triangular readout scheme. This method yields an independent chemical-shift dimension that contains, for each voxel, the NMR spectrum after the FT. Integration of the NMR spectrum over the resonance line of a given chemical compound yields the spatial image with the respective chemical-shift contrast.

B. Hadamard chemical-shift imaging

As an efficient alternative to Fourier encoding, Hadamard encoding can be used for the chemical-shift dimensions.[26,27] The Hadamard-CSI pulse sequence [Fig. 2(b)] yields images with one spectral and two spatial dimensions $F^{\mathrm{spa}}H_N^{\mathrm{spe}}H_{\mathrm{Mq}}^{\mathrm{spa}}$. After the gradient source is flipped away a nutation pulse for the rotating-frame encoding in the x dimension[28] is applied. This is followed by a spectral Hadamard encoding with frequency-selective hyperbolic secant pulses. For recording a full spectrum, both Hadamard and Fourier encoding are expected to yield the same SNR per time unit. A significant time savings can, however, be achieved with Hadamard encoding, if only a limited number N of resonances in the spectrum is present or is of interest.

In the following we apply Hadamard encoding schemes H_N with $N = 2,4,8$ (for the respective matrices, see the Appendix), for which the relation $H_N^T H_N = N I_N$ holds. Here I_N is the $N \times N$-identity matrix and H_N^T the transposed Hadamard matrix. Spectral Hadamard reconstruction is performed in the same manner as spatial Hadamard reconstruction using $P = H_N^T E$, where E is the detected Hadamard encoded spectrum and P the reconstructed spectrum. The spectral resolution of a Hadamard spectrum is limited by the excitation width of the Hadamard slice and, ultimately, by the homogeneous linewidth of the sample. For known chemical-shift positions the Hadamard slices can then be chosen such that each encompasses the spins at one separate resonance frequency only. With an appropriate selection of the Hadamard slices, several images with a chemical-shift contrast can be recorded simultaneously (e.g., the distribution of different chemical compounds). This is by far the fastest method for creating images with chemical-shift contrast if the chemical composition of the sample is known.

C. Quadrature detected spatial Hadamard encoding

Spatial Hadamard encoding is a multiplexing scheme that affords a higher SNR per unit time compared to conventional sequentially detected MRFM.[23] For sensitivity-limited measurements it significantly reduces the measurement time if the same SNR is to be achieved.[28,29] Here we show that spatial Hadamard encoding with a single-sided readout waveform allows quadrature detection of the cantilever oscillation. The resulting scheme yields the same spatial resolution as obtained for a Hadamard-N encoding but with only half the encoding steps.

In order to introduce this feature, we evaluate the point spread function of a single-sided readout waveform. Figure 3(a) shows the time evolution of the M_z magnetization during a sawtooth excitation, as a function of the Larmor frequency (encoding the spatial position) and the time. This corresponds to the step function $F_z \propto M_z$ [shown in Fig. 3(b)], which is the time-dependent force of spins with Larmor frequency ω. During the MRFM detection, the lock-in amplifier mixes down the signal with a $\cos(\omega_{\mathrm{can}}t)$ and a $\sin(\omega_{\mathrm{can}}t)$ reference signal, with the cantilever eigenfrequency ω_{can}. This then leads to the detected cantilever audio signal $S_z \propto F_z(\omega,t)\exp[i\varphi(\omega)]$, with the phase $\varphi(\omega) = \pi\omega/\Delta\omega_{\mathrm{rf}}$ and $\Delta\omega_{\mathrm{rf}}$ is the excitation bandwidth. For an encoding scheme within $2N$ slices, the phase difference between neighboring slices is $\Delta\varphi = \pi/(2N)$. The signals from two slices at positions n and $N+n$ will differ in phase by 90° and will be detected in the two quadrature channels, doubling the number of slices that can be detected in the same time.

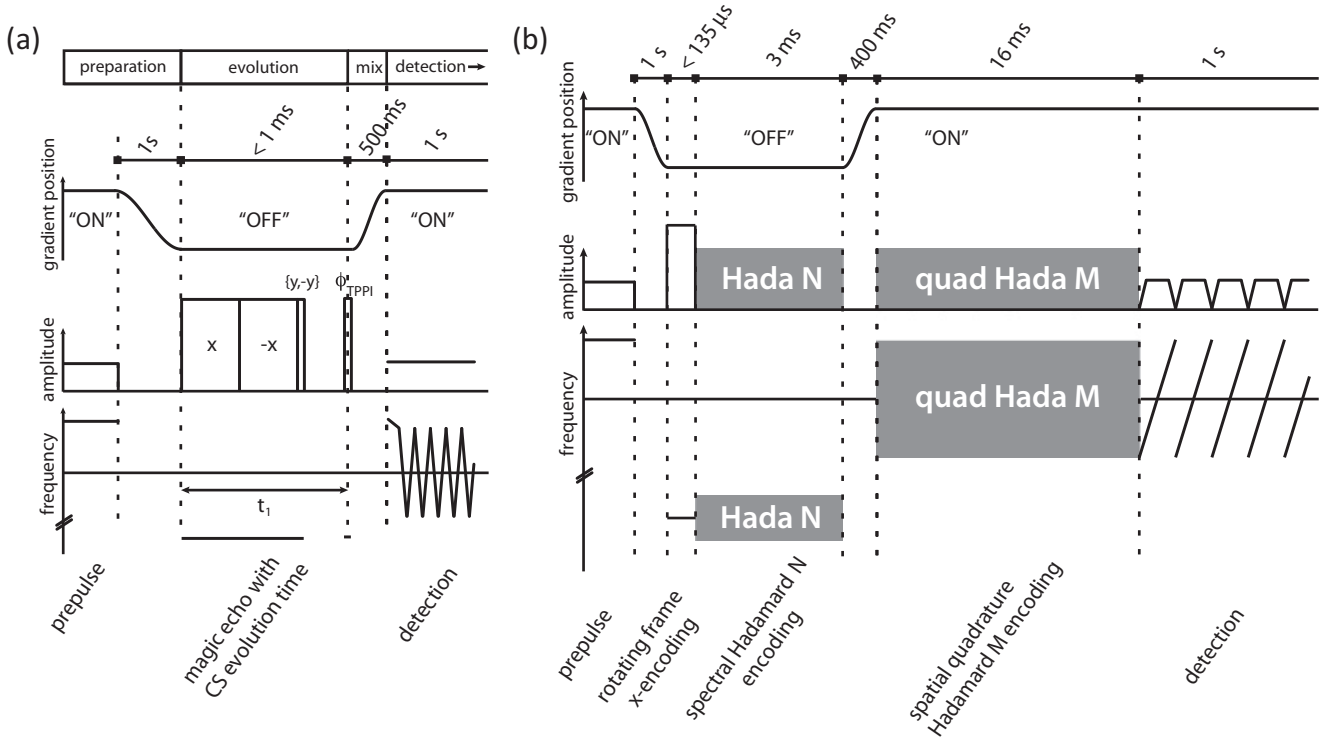

FIG. 2. Pulse sequences for mechanically detected chemical-shift imaging. For spectral encoding and Fourier spatial encoding the gradient is in the "off" position; otherwise, it is "on." The $F^{\mathrm{spe}}S$ experiment (a), consists of a t_1 evolution time combined with a magic echo[24] for homonuclear dipolar decoupling. (b) The encoding schematically depicts the $F^{\mathrm{spa}}H_N^{\mathrm{spe}}H_{Mq}^{\mathrm{spa}}$ experiment and turns into the $H_N^{\mathrm{spe}}H_{Mq}^{\mathrm{spa}}$ experiment if the "rotating-frame x encoding" is omitted. Hyperbolic secant pulses are used to accomplish the Hadamard encoding, which is applied only to a selected region of interest. A polarization cycle is applied in the H_N^{spe} dimension to remove experimental artifacts.

III. EXPERIMENTAL PROCEDURE

The experiments were performed with a home-built MRFM spectrometer and probe in high vacuum (10^{-3} mbar) at room temperature and in a 5.87-T wide-bore standard NMR magnet.[13,30] The probe is based on a sample-on-cantilever design with the oscillation in the direction of the main field B_0. A FeCo cylinder (300-μm diameter, $B_{\mathrm{sat}} = 2.3$ T) was used as the gradient source. In the preparation period a prepulse was applied far off-resonance from the readout frequency in order to minimize transients caused by cantilever electromagnetic heating. During the chemical-shift encoding this readout gradient was flipped away by a sheer piezo (Physikinstrumente), which can drive the gradient source up to 2 mm away from the sample position.[18] The phantom sample

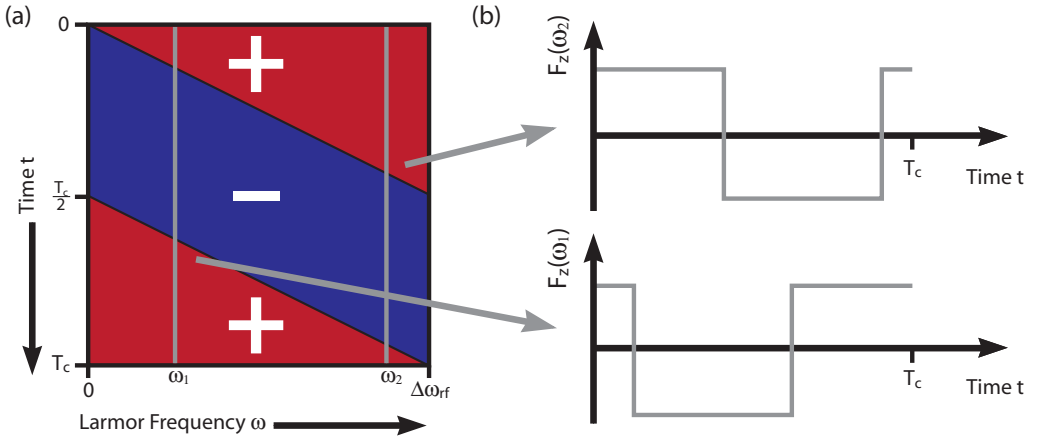

FIG. 3. (Color online) (a) Idealized frequency-dependent M_z magnetization obtained with single-sided excitation over one cantilever period T_c. The magnetization oriented parallel to the external magnetic field is shown in red; antiparallel magnetization, in blue. (b) Time-dependent force profile of the magnetization for spins with Larmor frequencies ω_1 and ω_2. In the MRFM detection process the resulting step function is projected onto the functions $\cos(\omega_{\mathrm{can}}t)$ and $\sin(\omega_{\mathrm{can}}t)$, which yields a phase shift of 180° between the two ends of the excitation bandwidth.

for the 2D measurements $F^{\mathrm{spe}}S$ and $H_N^{\mathrm{spe}}H_{Mq}^{\mathrm{spa}}$ consisted of one MgF_2 and two KPF_6 single crystals. The KPF_6 crystals were glued on top of the MgF_2 placed on a commercially available silicon-nitride cantilever ($k = 10$ mN/m, $Q \sim 8k$, $\nu_{\mathrm{can}} = 890$ Hz) (Veeco Probes). For the 3D experiment $F^{\mathrm{spa}}H_N^{\mathrm{spe}}H_{Mq}^{\mathrm{spa}}$, a MgF_2 crystal and a KPF_6 crystal were glued onto a custom-made silicon cantilever[31] ($k = 0.42$ mN/m, $Q \sim 5k$, $\nu_{\mathrm{can}} = 1080$ Hz). The rf field was generated by a 4.5-turn coil with a 200-μm inner diameter for the 2D and a 3.5-turn coil with a 100-μm inner diameter for the 3D experiment. The 100-μm coil was used as gradient coil for the x encoding.[28] The fluorine chemical-shift scale was referenced to the KPF_6 peak at -65 ppm.[32]

IV. RESULTS AND DISCUSSION

In order to demonstrate the features of CSI, a sample consisting of two single crystals, MgF_2 and KPF_6, was fabricated. A piece of KPF_6 crystal was glued on top of a smaller piece of MgF_2. The FT-CSI 1D spectra $F^{\mathrm{spe}}S$ of the phantom sample are shown in Fig. 4(a). The resulting chemical-shift dimension features two well-resolved lines from the two distinct ^{19}F species in the sample. From the 2D data, a 1D image with chemical-shift contrast (encoded by color) was constructed by integrating, over the respective peaks assigned to KPF_6 and MgF_2 [shown in Fig. 4(a) in red and green]. The data were recorded with the pulse sequence shown in Fig. 2(a). Due to the slow T_1 relaxation the interscan delay had to be set to 1 min, leading to a total measurement time of about 20 h. In the sample region farther away from the gradient source, only MgF_2 is present, which gives rise to the broader peak in the spectrum, while closer to the gradient source, in accordance with the sample preparation, the KPF_6 region is found, leading to the narrower line. The remaining inhomogeneity of the magnetic field, when the gradient is in the "off" position, was determined from the z-position dependence of the KPF_6 peaks to be 1.4 ± 0.1 kHz/MHz at the sample position. The spectra in Fig. 4(a) were corrected for this position-dependent shift by applying a shearing transformation.

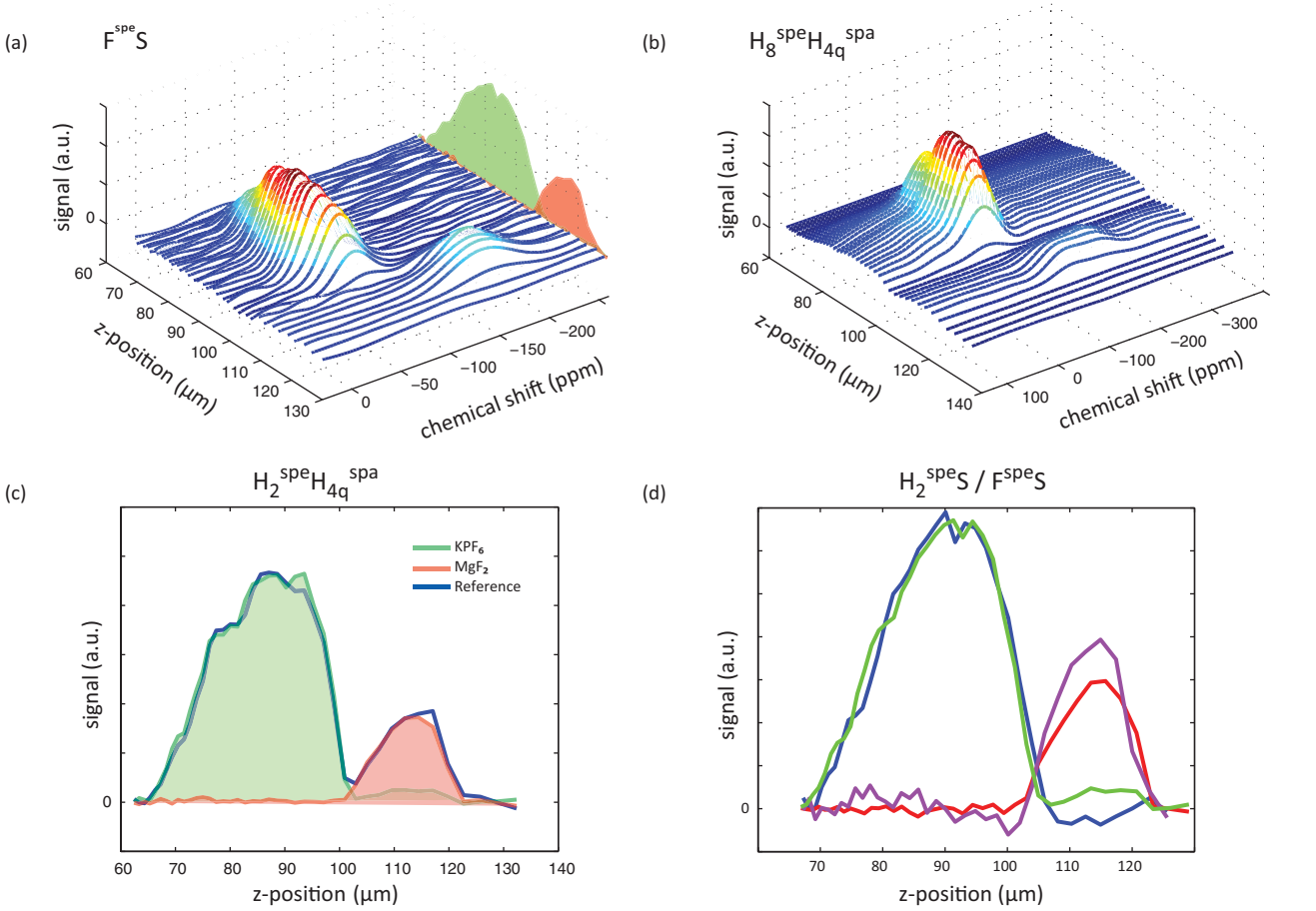

FIG. 4. (Color online) (a) Thirty-seven localized fluorine chemical-shift spectra ($F^{\mathrm{spe}}S$) of the phantom sample. The MgF_2 and KPF_6 peaks are virtually separated in both the spatial and the spectral dimensions. The KPF_6 peak has a narrower linewidth due to the smaller dipolar coupling. The red and green areas at the right represent integrals over the chemical-shift range of MgF_2 and KPF_6, respectively. (b) Hadamard-CSI spectrum $H_8^{\mathrm{spe}}H_{4q}^{\mathrm{spa}}$ of the same sample. Trigonometric interpolations of the eight spectral points were applied. (c) Chemical-shift resolved spatial 1D ^{19}F image $H_2^{\mathrm{spe}}H_{4q}^{\mathrm{spa}}$ of the phantom sample containing KPF_6 and MgF_2 crystals. The blue line represents the ^{19}F spin density from a 1D H_{4q}^{spa} reference experiment. The red and green lines represent the spin density corresponding to the MgF_2 and KPF_6 signals. (d) Comparison of the chemical-shift selective images obtained in a $H_2^{\mathrm{spe}}S$ and $F^{\mathrm{spe}}S$ experiment. The acquisition scheme differs only in the chemical-shift dimension. The KPF_6 is represented in green and blue and the MgF_2 signal in red and magenta for the $H_2^{\mathrm{spe}}S$ and $F^{\mathrm{spe}}S$ experiments, respectively.

The Hadamard-CSI 1D spectra of the same phantom sample are shown in Fig. 4(b). The $H_8^{\mathrm{spe}} H_{4q}^{\mathrm{spa}}$ experiment was recorded with the pulse sequence shown in Fig. 2(b) within 8 h. A resolution of 15 kHz was used with the spectral Hadamard-8 encoding. The results of the Hadamard-CSI and FT-CSI experiments are well reproduced. Compared to Fig. 4(a), the MgF_2 peak is significantly broader and less intense in the Hadamard-CSI in Fig. 4(b), because no homonuclear decoupling with the magic echo scheme can be applied.

As discussed in Sec. II, we may record a chemical-shift filtered image in a much shorter time by applying a Hadamard-2 encoding sequence. Using the pulse sequence of Fig. 2(b), an image was recorded without rotating-frame encoding. Figure 4(c) shows the results of the Hadamard-2 contrast experiment $H_2^{\mathrm{spe}} H_{4q}^{\mathrm{spa}}$, with both signals cleanly separated by the Hadamard encoding. Using this approach the measurement time for the chemical-shift contrast image could be greatly reduced, to only 2 h.

In Fig. 4(d) the chemical-shift contrast images obtained using $F^{\mathrm{spe}} S$ (blue and magenta) and $H_2^{\mathrm{spe}} S$ schemes (green and red) are compared. The shift-selective images obtained by the two methods are in excellent agreement. The signals are scaled such that the KPF_6 crystals have the same maximum intensities. Even small features like the dip in the middle of the KPF_6 crystal are well reproduced in both experiments. The MgF_2 signal in the $F^{\mathrm{spe}} S$ image is stronger than in the Hadamard image. We believe that this is because the inversion sweeps used in the Hadamard-2 is less efficient for MgF_2 than for KPF_6—as a result of the stronger dipole coupling—explaining the reduction in signal amplitude.

To extend the 1D Hadamard-CSI experiments (2D data), a 3D experiment $F^{\mathrm{spa}} H_8^{\mathrm{spe}} H_{8q}^{\mathrm{spa}}$, containing a 2D spatial image and a chemical-shift dimension, was performed using a different phantom sample but with the same two compounds, KPF_6 and MgF_2. The planes in Fig. 5(a) represent the eight spectral slices and show the spatial distribution within a slice. Conversely, for each spatial grid point a chemical-shift spectrum with a resolution of 15 kHz (64 ppm) is represented. Figure 5(a) shows that the sample again consisted of two spectrally separated peaks. The two peaks have different spatial distributions, corresponding to the different sample positions. The MgF_2 crystal (lower chemical shift) is smaller and, furthermore, shows a lower signal intensity due to the smaller crystal size and the larger linewidth (see also Fig. 4). The measurement time for the entire 3D image was 2 days 7 h, which was again mainly determined by the interscan delay of 60 s needed because of the slow relaxation of this particular sample. The measurement time will scale linearly with a shortened relaxation time, e.g., by paramagnetic doping. Due to the combination of spectral Hadamard, rotating-frame Fourier and quadrature-detected Hadamard encoding all dimensions benefited from multiplexing. No additional signal averaging was needed.[33,34]

As before, knowing the spectrum, a Hadamard-2 scheme can be used in the chemical-shift dimension to obtain a 2D spatial image with chemical contrast (3D $F^{\mathrm{spa}} H_2^{\mathrm{spe}} H_{8q}^{\mathrm{spa}}$). The resulting images of KPF_6 and MgF_2 (green and red) are shown in Fig. 5(b). The measurement time for this data set was 14 h. Figure 5 clearly shows that the two crystals used had different shapes and sizes. The smaller MgF_2 crystal sat on top of the KPF_6 crystal and this crystal was significantly smaller.

Finally, the images shown in Fig. 4 have a spatial resolution for the FT-CSI and spatial 1D Hadamard-CSI experiments of 1–3 μm in the z direction. This resolution was chosen in order to limit the measurement time for imaging the roughly 60-μm-sized object. The spatial resolution in the z direction of these experiments could easily be reduced to under 1 μm by choosing smaller readout widths. The z resolution of the smaller phantom sample in the spatial 2D Hadamard-CSI experiment shown in Fig. 5 was 600–800 nm. The resolution

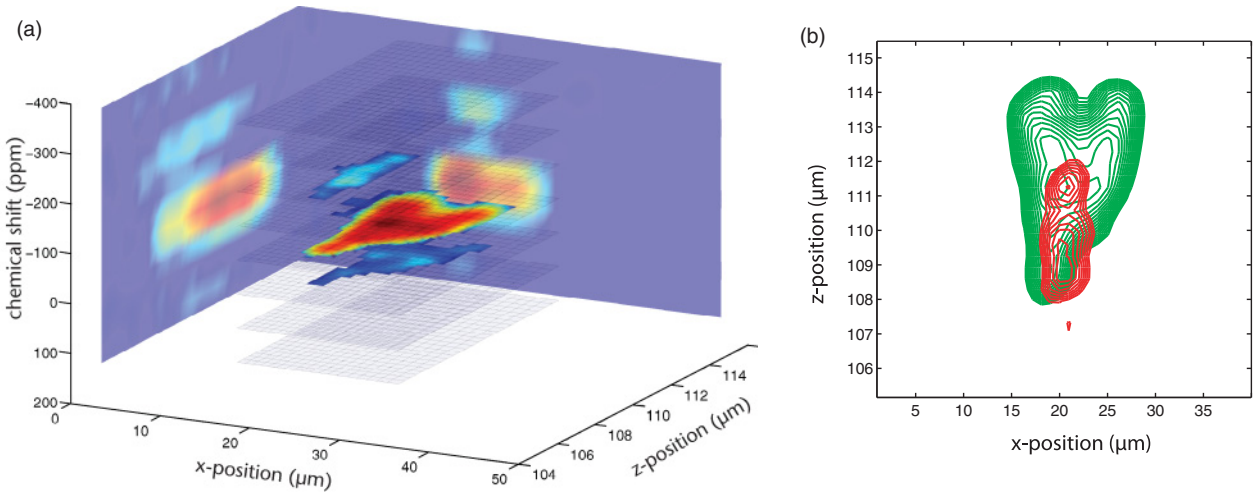

FIG. 5. (Color online) (a) 3D image $F^{\mathrm{spa}} H_8^{\mathrm{spe}} H_{8q}^{\mathrm{spa}}$ of a sample containing KPF_6 and MgF_2, with a 1D spectral dimension combined with a spatial 2D ^{19}F image. The planes represent the eight spectral slices and show the spatial distribution within a slice. The intensities of the planes are projected along each spatial dimension. Projections were trigonometrically interpolated to 16 points. Intensities of the spectral planes as well as of the projections are plotted with a logarithmic color scaling. (b) Chemical-shift resolved spatial 2D ^{19}F image $F^{\mathrm{spa}} H_2^{\mathrm{spe}} H_{8q}^{\mathrm{spa}}$ of the same sample. The red and green contour lines represent the spin density in the spectral range located up to 50 kHz to each side of the carrier frequency, allowing discrimination of MgF_2 (red) and KPF_6 (green) signals. The z position is referenced to the distance from the gradient source.

along the x dimension was 3.2–4.4 μm, which was limited by the rf gradient strength produced by our coil.

V. CONCLUSION

We have shown that the chemical shift can be used for MRFM CSI as well as for image contrast in nanoscale MRI images. As a significant extension of an earlier study,[18] examples presented here involve not only 1D but also 2D spatial images, with the option to be extended to 3D spatial images by adding a second gradient coil perpendicular to the main B field and the first coil.

Both Fourier encoding and the newly introduced Hadamard encoding schemes have been used in the spectral dimensions and have been shown to be effective. Hadamard and Fourier encoding both benefit from multiplexing and therefore have, for identical spectra with the same resolution, the same SNR per unit time. The FT-CSI experiment can be combined with homonuclear spin decoupling (e.g., magic-echo sequences) and leads to narrower resonance lines in the case of a dipole-limited linewidth. Due to the capacity to tailor them to known spectra, Hadamard encoding is particularly advantageous for spectra with a few resonances and spectra with many empty intervals.[26]

The experiments described not only introduce multiplexing schemes for all dimensions—in contrast to earlier schemes—but also introduce quadrature-detected spatial Hadamard encoding, which allows further cutting of the measurement time, in half, in analogy with quadrature detection in NMR spectroscopy,[35,36] and can be useful for multidimensional experiments. The measurement times could be shortened significantly if the T_1 relaxation times could be shortened, which may be the case for other samples or could be achieved by paramagnetic doping.

The resolution of our images is of the order of hundreds of nanometers. We are clearly in a regime where the observation of Zeeman magnetization is much more sensitive than the statistical polarization which was used for the observation of very highly resolved pictures at cryogenic temperatures.[11] While our resolution could be improved using higher B_0 and B_1 field gradients, the reduction of the voxel size to 10 nm seems, for sensitivity reasons, realistic only at cryogenic temperatures. Some of the principles, in particular, quadrature detection, could, however, also be applied in the context of working with statistical polarization and at low temperatures.

APPENDIX: HADAMARD MATRICES

$$H_2 = \begin{pmatrix} 1 & 1 \\ 1 & -1 \end{pmatrix}.$$

$$H_4 = \begin{pmatrix} 1 & 1 & 1 & 1 \\ 1 & 1 & -1 & -1 \\ 1 & -1 & 1 & -1 \\ 1 & -1 & -1 & 1 \end{pmatrix}.$$

$$H_8 = \begin{pmatrix} 1 & 1 & 1 & 1 & 1 & 1 & 1 & 1 \\ 1 & 1 & 1 & 1 & -1 & -1 & -1 & -1 \\ 1 & 1 & -1 & -1 & 1 & 1 & -1 & -1 \\ 1 & 1 & -1 & -1 & -1 & -1 & 1 & 1 \\ 1 & -1 & 1 & -1 & 1 & -1 & 1 & -1 \\ 1 & -1 & 1 & -1 & -1 & 1 & -1 & 1 \\ 1 & -1 & -1 & 1 & 1 & -1 & -1 & 1 \\ 1 & -1 & -1 & 1 & -1 & 1 & 1 & -1 \end{pmatrix}.$$

*beme@ethz.ch; www.ssnmr.ethz.ch

[1] P. C. Lauterbur, Angew. Chem.-Int. Ed. **44**, 1433 (2005).
[2] T. Brown, B. Kincaid, and K. Ugurbil, Proc. Natl. Acad. Sci. USA **79**, 3523 (1982).
[3] L. Ciobanu, D. A. Seeber, and C. H. Pennington, J. Magn. Reson. **158**, 178 (2002).
[4] P. Glover and P. Mansfield, Rep. Prog. Phys. **65**, 1489 (2002).
[5] J. A. Sidles, Appl. Phys. Lett. **58**, 2854 (1991).
[6] J. A. Sidles, Phys. Rev. Lett. **68**, 1124 (1992).
[7] D. Rugar, C. S. Yannoni, and J. A. Sidles, Nature **360**, 563 (1992).
[8] D. Rugar, O. Zuger, S. Hoen, C. S. Yannoni, H. M. Vieth, and R. D. Kendrick, Science **264**, 1560 (1994).
[9] J. A. Sidles and D. Rugar, Phys. Rev. Lett. **70**, 3506 (1993).
[10] D. Rugar, R. Budakian, H. J. Mamin, and B. W. Chui, Nature **430**, 329 (2004).
[11] C. L. Degen, M. Poggio, H. J. Mamin, C. T. Rettner, and D. Rugar, Proc. Natl. Acad. Sci. USA **106**, 1313 (2009).
[12] A. Abragam, *The Principles of Nuclear Magnetism* (Clarendon Press, Oxford, 1961).
[13] C. L. Degen, Q. Lin, A. Hunkeler, U. Meier, M. Tomaselli, and B. H. Meier, Phys. Rev. Lett. **94**, 207601 (2005).
[14] C. L. Degen, Q. Lin, and B. H. Meier, Phys. Rev. B **74**, 104414 (2006).
[15] Q. Lin, C. L. Degen, M. Tomaselli, A. Hunkeler, U. Meier, and B. H. Meier, Phys. Rev. Lett. **96**, 137604 (2006).
[16] K. W. Eberhardt, Q. Lin, U. Meier, A. Hunkeler, and B. H. Meier, Phys. Rev. B **75**, 184430 (2007).
[17] R. Verhagen, A. Wittlin, C. W. Hilbers, H. van Kempen, and A. P. M. Kentgens, J. Am. Chem. Soc. **124**, 1588 (2002).
[18] K. W. Eberhardt, C. L. Degen, A. Hunkeler, and B. H. Meier, Angew. Chem. Int. Ed. Engl. B **47**, 8961 (2008).
[19] G. M. Leskowitz, L. A. Madsen, and D. P. Weitekamp, Sol. St. NMR **11**, 73 (1998).
[20] L. Bolinger and J. S. Leigh, J. Magn. Reson. **80**, 162 (1988).
[21] G. Goelman, V. H. Subramanian, and J. S. Leigh, J. Magn. Reson. **89**, 437 (1990).
[22] G. Goelman and J. S. Leigh, J. Magn. Reson. **91**, 93 (1991).
[23] K. W. Eberhardt, C. L. Degen, and B. H. Meier, Phys. Rev. B **76**, 180405 (2007).
[24] W. K. Rhim, A. Pines, and J. S. Waugh, Phys. Rev. B **3**, 684 (1971).

[25]R. R. Ernst, G. Bodenhausen, and A. Wokaun, *Principles of Nuclear Magnetic Resonance in One and Two Dimensions* (Clarendon Press, Oxford, 1987).
[26]E. Kupce and R. Freeman, J. Magn. Reson. **162**, 158 (2003).
[27]E. Kupce, T. Nishida, and R. Freeman, Prog. Nucl. Magn. Reson. Spectrosc. **42**, 95 (2003).
[28]K. W. Eberhardt, A. Hunkeler, U. Meier, J. Tharian, S. Mouaziz, G. Boero, J. Brugger, and B. H. Meier, Phys. Rev. B **78**, 214401 (2008).
[29]K. W. Eberhardt, S. Mouaziz, G. Boero, J. Brugger, and B. H. Meier, Phys. Rev. Lett. **99**, 227603 (2007).
[30]C. L. Degen, U. Meier, Q. Lin, A. Hunkeler, and B. H. Meier, Rev. Sci. Instrum. **77**, 043707 (2006).
[31]S. Mouaziz, G. Boero, G. Moresi, C. L. Degen, Q. Lin, B. H. Meier, and J. Brugger, Microelectron. Eng. **83**, 1306 (2006).
[32]T. M. Duncan, *A Compilation of Chemical Shift Anisotropies* (Farragut Press, Chicago, IL, 1990).
[33]J. C. Hoch, A. S. Stern, D. L. Donoho, and I. M. Johnstone, J. Magn. Reson. **86**, 235 (1990).
[34]M. Lustig, D. Donoho, and J. M. Pauly, Magn. Reson. Med. **58**, 1182 (2007).
[35]A. G. Redfield and R. K. Gupta, J. Chem. Phys. **54**, 1418 (1971).
[36]A. G. Redfield and R. K. Gupta, Adv. Magn. Reson. **5**, 81 (1971).